Article

Plasmon Chemistry on Ag Nanostars: Experimental and Theoretical Raman/SERS Study of the Pesticide Thiacloprid Bond Cleavage by the Plasmon Deactivation Effect

Freddy Celis,* Andrés Aracena, Macarena García, Rodrigo Segura del Río, Santiago Sanchez-Cortes, and Patricio Leyton

Read Online

ACCESS | ⅰⅼⅼ Metrics & More | 📰 Article Recommendations | 🆂🅸 Supporting Information

ABSTRACT: Silver nanoparticles (AgNPs) were synthetized and employed in surface-enhanced Raman scattering measurements to study the chemical behavior when thiacloprid (Thia) interacts with the surface of Ag nanospheres (AgNSp) and Ag nanostars (AgNSt) upon excitation of the system with a 785 nm laser. Experimental results show that the deactivation of the localized surface plasmon resonance induces structural changes in Thia. When AgNSp are used, it is possible to observe a mesomeric effect in the cyanamide moiety. On the other hand, when AgNSt are employed, it promotes the cleavage of the methylene ($-CH_2-$) bridge in Thia to produce two molecular fragments. To support these results, theoretical calculations based on topological parameters described by the atoms in molecules theory, Laplacian of the electron density at the bond critical point ($\nabla^2\rho$ BCP), Laplacian bond order, and bond dissociation energies were made, confirming that the bond cleavage is centered at the $-CH_2-$ bridge in Thia.

AgNSt + Thia + 785 nm = Plasmon induced reaction
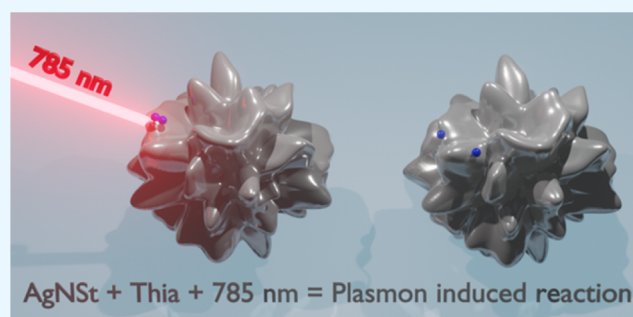
INTRODUCTION

The fact that insect pests become resistant to many chemical compounds has led to the constant development of chemical synthetic strategies to produce pesticides or persistent organic pesticides (POPs) that can control them. One of these chemical developments is the neonicotinoid (NeN) neuro-active insecticide group that is widely employed in farming around the world. The main problem of NeNs is that they present undesirable effects over the environment and human health because of their persistence.[1,2] In particular, thiacloprid (Thia) ((Z)-[3-[(6-chloro-3-pyridinyl)methyl]-2-thiazolidinylidene]cyanamide), a cyanoimine NeN compound, was recently been identified as an agent that causes DNA damage in the adult zebrafish model organism[3] and transcriptional changes in mitochondria-related genes in honey bees.[4] As a result of these studies, this compound is being proposed as a genotoxic agent, where its persistence is attributed to its low absorptivity of UV light and higher better photostability in comparison to other NeNs.

Currently, there are two general strategies to reduce or degrade this type of compound: (i) reduction of pesticide levels in the environment through membrane filtration,[5,6] surface adsorption,[7,8] or biological degradation[9,10] and (ii) degradation of pesticides by chemical methods such as electrochemical,[11−13] organic photocatalysis,[14] radicals such as oxidizing agents,[15] photochemical,[16] and photolysis,[17−19] among others. However, all these methods can potentially generate chemical species that could be more toxic than the initial precursor.

An alternative method for the pesticide elimination in the environment is the use of nanotechnology, such as nanoparticles (NPs),[20,21] nanocomposites,[21,22] metal NPs,[23,24] bimetallic NPs,[25,26] and metal oxide NPs.[27,28] Some nanomaterials that display plasmonic effects are very promising in the photoinduced POP degradation. One of the most outstanding properties of these nanomaterials is that they can support localized surface plasmons (LSPs) that can be excited by using a light of an adequate wavelength, leading to LSP resonance (LSPR), which is an effect derived from the interaction of the resonant radiation with the free electrons. The deactivation of the LSPR absorbed energy by the metal may lead to nonradiative energy transfer to the adsorbed molecule with a great deal of physical and chemical applications.[29] On the other hand, the radiative deactivation of LSPR leads to the surface-enhanced Raman scattering (SERS) effect due to a considerable enhancement of the electric field proximal to
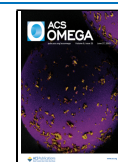
the surface. SERS has become a current tool in the analysis of pollutant traces by adsorbing the pollutants onto noble metal NPs, causing changes in the Raman spectrum depending on interactions with the metal surface and according to the SERS selection rules.[30]

Particularly, the deactivation of the LSPR by the non-radiative way is the basis of plasmon chemistry (PCh), which is an emerging science dealing with the induction of chemical reactions on the surface of NPs.[31−33] Some examples of PCh are demethylation and decomposition of methylene blue,[34−36] N=N bond formation in aminothiophenol derivatives,[22,37,38] S−S bond dissociation in dimethyl disulfide,[39] and dehalogenation rate of bromoadenine.[33] Four mechanisms involved in PCh were proposed to account for the chemical effects: direct intramolecular excitation (DIE), charge transfer (CT), indirect hot-electron transfer (IHET), and local heating. Two of these mechanisms, DIE and CT, are closely related to two spectroscopic techniques, resonance Raman spectroscopy and SERS, respectively.[40] This consideration is relevant since it supports Raman spectroscopy as the suitable spectroscopic tool to study a structural modification in any system, based on the possibility of following the reaction coordinate from the changes in a Raman or SERS spectral profile. In this sense, silver is one of the most used noble metals to prepare diverse nanostructures to be used in the enhancement of the Raman profile, in PCh studies, or even in other fields of science.[41−46]

In the present work, we have employed Ag nanostars (AgNSt) to induce the PCh-mediated degradation of the surface-immobilized Thia. The enhancement of the Raman signals by the plasmon effect was employed to understand the specific chemical interactions established between the metal and the adsorbed pesticide as well as the structural changes associated with the degradation process by PCh. For this reason, we have synthetized AgNSt and Ag nanospheres (AgNSp) to study the plasmonic effects. The SERS spectra of Thia adsorbed on AgNSt were compared with those obtained on AgNSp and to the regular Raman spectra in order to analyze the degradation effect caused by the presence of these NPs and laser radiation. Furthermore, theoretical calculations based on density functional theory (DFT) and topological parameters described by the AIM theory were done in order to propose a mechanism for the chemical degradation of Thia once adsorbed onto the metal surface.

■ MATERIALS AND METHODS

All the chemical reagents were of analytical grade and used without any further purification. Thia, silver nitrate, sodium hydroxide, hydroxylamine solution, and hydroxylamine hydrochloride were purchased from Sigma-Aldrich. Ultrapure water type 1 (1.8 μS) from the Simplicity water purification system was employed in the preparation of the NPs and the stock solutions.

Synthesis of AgNPs. AgNSp and AgNSt were synthesized following previously reported methods.[47,48] AgNSp were prepared by adding 300 μL of sodium hydroxide (1.0 M) to 90 mL of hydroxylamine hydrochloride (1.49 × 10^{-4} M). Then, 10 mL of silver nitrate (1.0 × 10^{-2} M) was added under rapid stirring conditions at room temperature, rendering a gray-reddish suspension. AgNSt were prepared according to a chemical reduction method, based on the reduction of the Ag$^+$ ion with neutral hydroxylamine and sodium citrate in two steps. First, 500 μL of sodium hydroxide (5 × 10^{-2} M) was mixed with 500 μL of hydroxylamine (6.02 × 10^{-2} M). Then,

9 mL of silver nitrate (1 × 10^{-3} M) was added dropwise to the solution. The resulting solution was stirred during 5 min. Finally, 100 μL of 4.13 × 10^{-3} M trisodium citrate was added. The final suspension was stirred for 15 min and immediately used.

Characterization of AgNPs by Scanning Electron Microscopy and Zeta Potential Measurements. The obtained AgNPs were characterized by scanning electron microscopy (SEM) to determine their morphology, as well as their electrokinetic potential was determined by measuring the zeta potential (ζP) of each nanoshape. For the SEM measurements, 10 μL of each sample suspension was dropped on silicon chips and left to dry in vacuum conditions. The measurements were performed in an ESEM Quattro S (Thermo Fisher Scientific), at 30 keV accelerating voltage and using an Everhart−Thornley secondary electron detector. The ζP was determined using the Nano ZS instrument (Malvern, UK) employing a fixed backscatter detector angle of 173° with the cell holder maintained at 25 °C. The Smoluchowski approximation (for aqueous solution) was used to calculate the ζP based on the measured electrophoretic mobility. The determined ζP was the result of at least three acquisition steps, with an average of 100 measurements for each step.

UV−Visible Spectra of Thia, AgNPs, and Thia-AgNPs. UV−visible absorption spectra of Thia, AgNP, and Thia-AgNP solutions were recorded from a Jasco V-530 spectrophotometer by using quartz cells with 1.0 cm optical path and a spectral resolution of 2 nm. The spectra of the solutions were registered from 190 to 1100 nm. The solutions of Thia and AgNPs were prepared by diluting 100 μL of Thia (1 × 10^{-4} M) or AgNPs in 1.9 mL of ultrapure water. In the case of Thia-AgNPs, 100 μL of Thia and 100 μL of AgNPs were mixed and added to 1800 μL of ultra-pure water.

Raman and SERS Spectra. The Raman and SERS spectra of all samples were recorded by using a micro-Raman system (RM1000, Renishaw) equipped with the 785 nm laser line, a Leica microscope, and a Peltier-cooled charge coupled device detector. The laser power on the Ag colloidal coated samples was 0.92 mW (1%) measured in situ. The instrument was calibrated using the 520 cm^{-1} band of a Si wafer and a 50× objective. Spectra were recorded by 1 scan using an integration time of 20 s and a spectral resolution at 4 cm^{-1}. To obtain the Raman spectrum of Thia, an aliquot of 100 μL of a Thia solution (1.0 × 10^{-4} M) was deposited on a gold thin surface and left to dry at room temperature. The thin Au film on the glass substrate was prepared by the sputtering method and used to avoid the intrinsic fluorescence emission of Thia that may interfere with the Raman spectrum. SERS spectra were recorded on a gold surface that was modified in different regions with 50 μL of AgNP solution and left to dry in air. After dry time, 10 μL of Thia solution (1 × 10^{-5} M) was added. The Thia droplet was then dried at room temperature in the absence of light.

Theoretical Aspects. Theoretical calculations were carried out by using Gaussian 09 (Revision E.01) software.[49] Vibrational frequencies of Thia were obtained using the DFT method, Becke, 3-parameter, Lee−Yang−Parr (B3LYP) functional, and basis set 6-311G(d,p) for an optimized structure of the pesticide employing the X-ray CIF file geometry, as shown in ref 50 The frequencies calculated for the theoretical Raman spectrum do not show any negative value, indicating that the optimized structure corresponds to the one at the minimum of
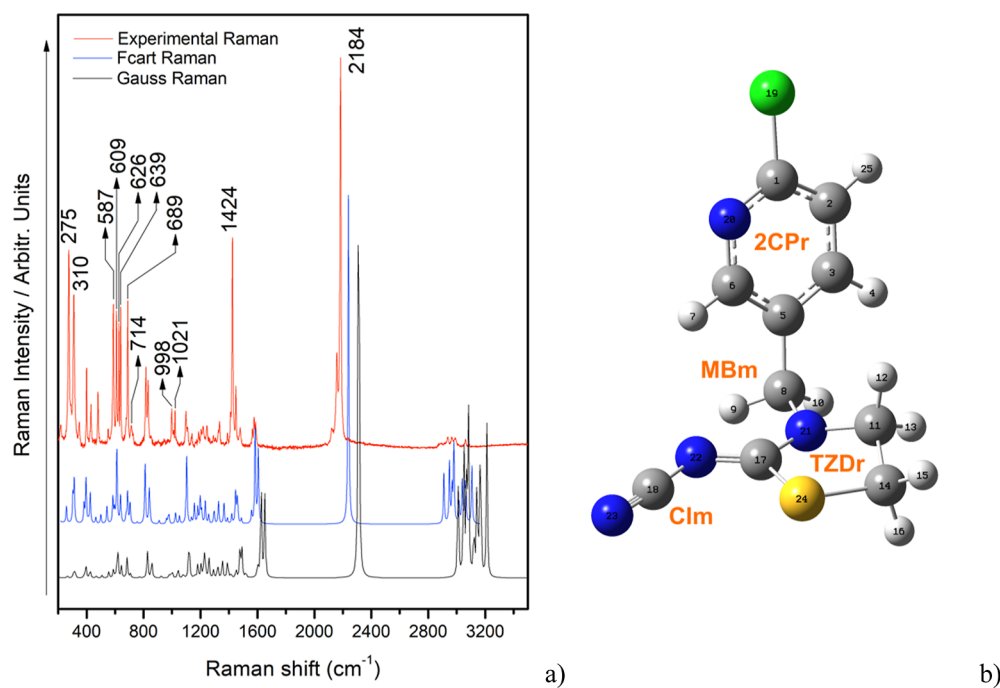
Figure 1. (a) Experimental [red(—)], theoretical scaled [blue(—)], and theoretical unscaled (—) Raman spectra of Thia. (b) Simulated structure of Thia from the CIF file by using DFT theoretical calculation with the corresponding acronym for each molecular group.

the potential energy surface. In other words, the optimized structure does not correspond to a transition state, and it is more alike to the real structure of Thia; therefore, the theoretical Raman spectrum is similar to the experimental Raman spectrum.[51] After obtaining the theoretical force constants (FCs) with Gaussian 09 software, by using FCART 7 (and according to the basis set used in the original calculation), the FCs were transformed into internal FCs and the obtained scale factor applied to the original theoretical vibrational frequencies was calculated by the same software.[52] Thia on the Ag surface was optimized by fixing Ag atoms with the previous methodology of calculation but using the Los Alamos National Laboratory 2 double-ζ (LANL2DZ) basis set. On the other hand, fragments of Thia onto the Ag surface were optimized by the same methodology described.[51] Properties based on the AIM theory were obtained with Multiwfn software version 3.3.6.6 using the fchk output file from Gaussian 09 as an input file.[53]

RESULTS AND DISCUSSION

Theoretical and Experimental Raman Spectra of Thia.
Theoretical Raman frequencies of Thia were calculated from the crystallographic structure of the pesticide available as a CIF file[50] to work with theoretical data obtained from the real structure of the compound. These results were treated employing FCART 7 software[52] because we considered that this methodology is more accurate than using specific scale factors applied to specific regions in the Raman spectrum. Using the scaled quantum mechanical method, the calculated cartesian FC matrix (CFCM) can be transformed into the internal coordinate system. This methodology allows the correction of errors in CFCM calculation by applying an appropriate scale factor to the internal coordinate. Table S1 displays the scale factors found by the above system for the different vibrational modes as well as the potential energy distribution for selected signals. The unscaled and scaled

theoretical Raman spectra are presented in Figure 1a. It is important to mention that the Raman and SERS assignments of the pesticide have been previously published.[54] In this sense, our data will complement what has been reported by the authors.

The experimental Raman spectrum of Thia, Figure 1a, does not display fluorescence interferences and shows characteristics medium-strong bands observed at 275, 310, 587, 609, 626, 639, 689, 1424, and 2184 cm^{-1}. In general, the very intense signal at 2184 cm^{-1} is attributed to the C≡N stretching mode and can be employed to follow any interaction between the Thia and silver surface because the strong Raman relative intensity of the latter band is associated with the relatively high polarizability of the cyanamide group.[55] This band is very useful to follow any structural change in terms of bond cleavage because this functional group is a representative of Thia. However, other signals will be also employed for the same aim as the band observed at 1424 cm^{-1} is attributed to the deformation of the —CH$_2$— bridge.[56] This group is sensitive to the chemical environment of the 2-chloropyridine and thiazolidine groups, due to a possible inductive electronic effect over the methylene (—CH$_2$—) group. This fact is verifiable according to the relative strong intensity of the Raman signal, as it also occurs in the case of the C≡N group. Thiazolidine ring (TDZr) and 2-chloropyridyl ring (2CPr) have specific Raman bands. Related to the thiazolidine ring, the symmetric and asymmetric stretching modes of C—S—C are observed at 714 and 689 cm^{-1} in the Raman spectrum, where the second signal has a medium-strong relative intensity due to the high polarizability,[57] similar to the case of the C≡N group. The signals assigned to the breathing mode of the 2-chloropyridyl ring are located at 1021 and 998 cm^{-1}. The identification of specific signals ascribed to TZDr, 2CPr, cyanoimine moiety (CIm), and methylene bridge moiety (MBm) (Figure 1b) will allow us to understand the chemical interactions between NP and the adsorbed Thia. In addition,
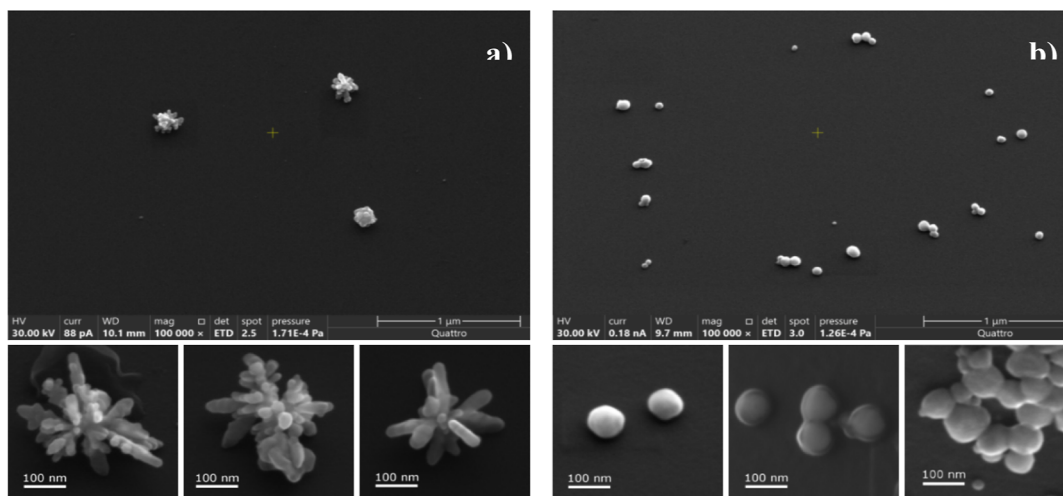
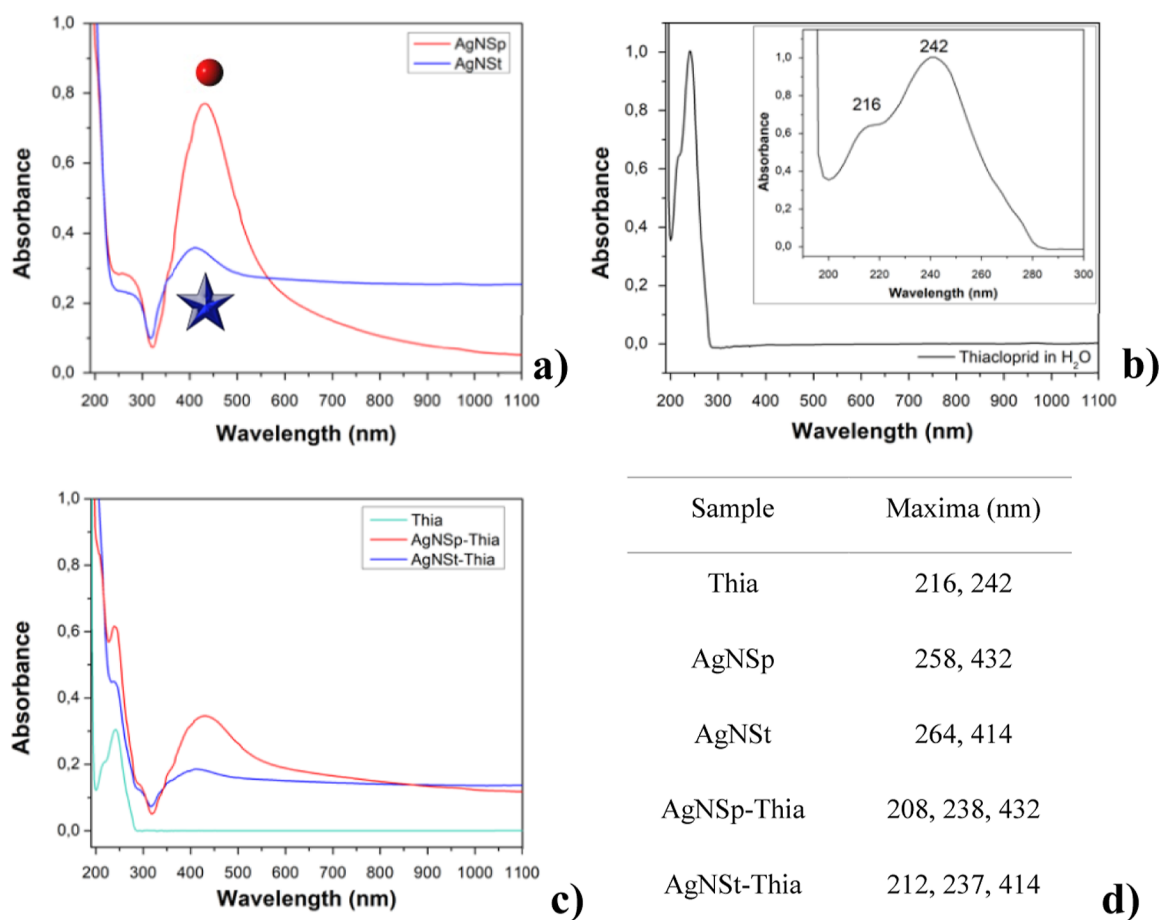**Figure 2.** High-resolution SEM images of (a) AgNSt and (b) AgNSp.

Figure 3. UV−visible spectra of (a) Ag NPs, (b) Thia, and (c) AgNPs + Thia (10^{-5} M) compared with Thia. (d) UV−visible maxima absorption band of Thia, AgNSp, AgNSt, and AgNPs-Thia.

the changes in the SERS spectrum will serve to understand any structural changes associated with the degradation process. The Raman assignment based on our theoretical calculation is available in the Supporting Information in Table S2.

Characterization of NPs and UV−Visible Absorption Spectra of Thia, NPs, and NPs-Thia. The obtained NPs were characterized by their morphological shape, electrokinetic potential, and their plasmonic activity in the UV−visible

spectrum. The images obtained by SEM show two different shapes depending on the chemical method used in their synthesis. Figure 2a displays star-like silver NPs (AgNSt), prepared by the two-step reduction with hydroxylamine and sodium citrate, and results are consistent with a previous report.[48,58] (Garcia-Leis et al., 2017). Those AgNSt present irregular shapes with sizes ranging 200−300 nm as they can be observed in the high-resolution images. On the other hand,
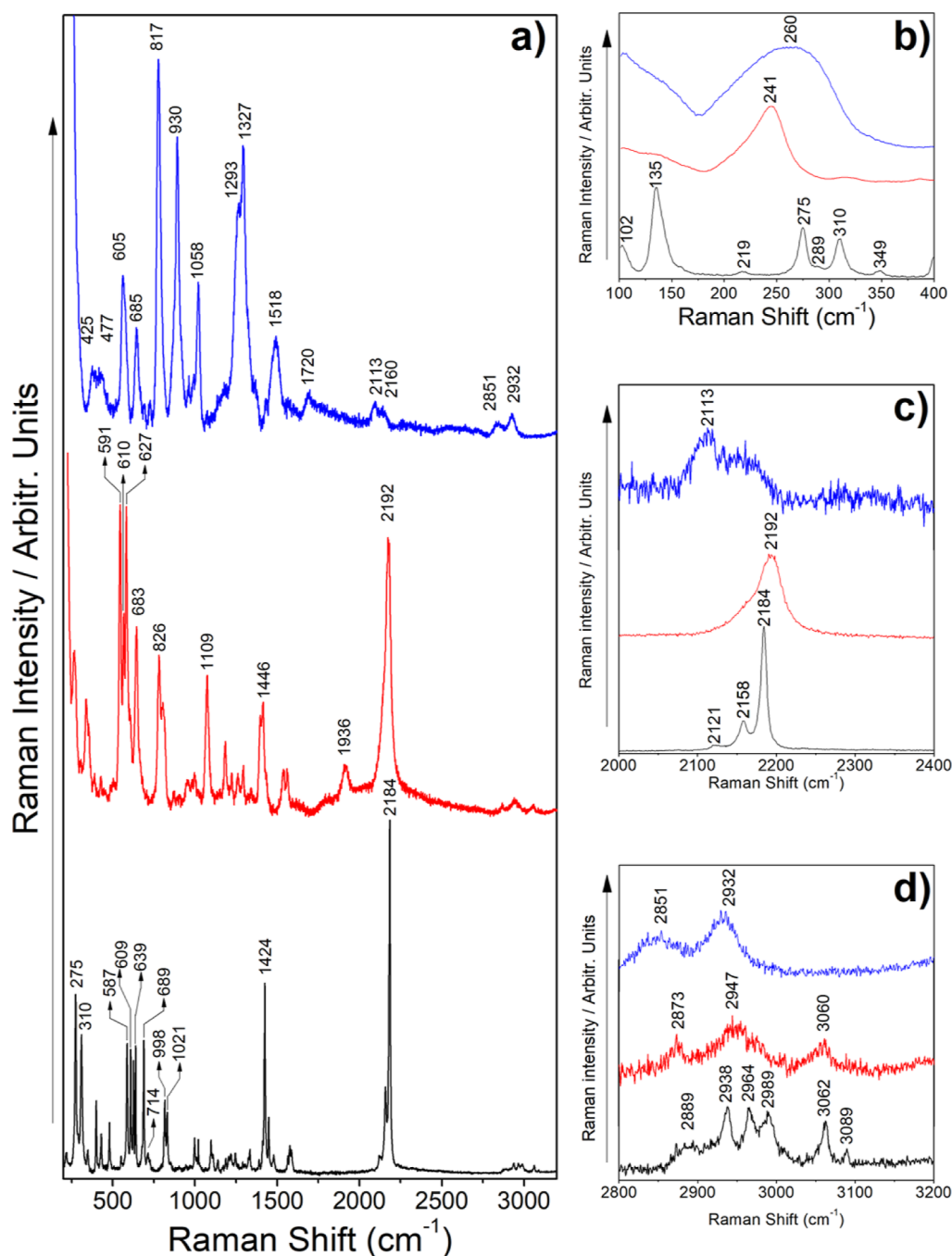
Figure 4. (a) Comparison of the Raman (—) spectrum of Thia with the SERS spectra onto the AgNSp [red(—)] and AgNSt [blue(—)]. Comparison of Raman/SERS spectra in the selected region: (b) 100−400, (c) 2000−2400, and (d) 2800−3200 cm^{-1}.

Figure 2b shows the spherical silver NPs (AgNSp) obtained by reduction with hydroxylamine hydrochloride, and results are in agreement with the report used as ref 47 The sizes of the obtained AgNSp are distributed between 30 and 90 nm, with an average size close to 60 nm. Values of ζP obtained were −10.9 mV for AgNSp and −41.9 mV for AgNSt, consistent with the different methods of preparation, leading to different capping agents and concentrations. The extinction spectra of AgNSp and AgNSt (Figure 3a) are related to the LSPR resonances observed for these NPs. These maxima appear at 432 nm in the case of AgNSp and at 414 nm for AgNSt NPs according to the corresponding reported morphology.[47,58] The different position of the maxima is due to each morphology

and size of the integrating NPs. In the case of the AgNSt, it is possible to observe a large extinction above 500 nm, which is consistent with the star shape. This shows the existence of a rather inhomogeneous distribution of sizes and morphologies, including the number of arms and the sharpness of their tips.[58] The different extinction spectra allow us to determine the most appropriate excitation wavelength to obtain the SERS spectra. According to the plasmon extinction results, AgNSt is a good candidate for both SERS and PCh effects due to its broader and intense LSPR in the red and near-infrared region of the electromagnetic spectrum. The 785 nm laser line was chosen due to its low energy and proximity to the IR region and because of the resonance with the plasmonic tail. Another

advantage of AgNSt is the fact that it is not necessarily a previous aggregation of NPs to induce the formation of hot spots, as in the case of the AgNSp. On the other hand, the UV−visible profile of Thia in aqueous solution (Figure 3b) shows two absorption bands at 216 and 242 nm that are also visible in the mixture (Figure 3c).

The LSPR maximum on each absorption profile in the NPs-Thia systems (Figure 3c) does not show any red or blue shift. Therefore, the changes in the density of free electrons in NPs due to the adsorption of Thia are negligible.[59] On the other hand, a hypsochromic shift is evidenced in Thia absorption bands (Figure 3d) because of the adsorption and the formation of a metal-Thia complex which promotes a new electronic distribution in the Thia structure.

SERS Spectra of Thia: Spectral Description. The SERS spectra of Thia (10^{-5} M) employing AgNSp and AgNSt are displayed in Figure 4a. The spectrum of Thia on AgNSp is very close to the reported data[54] with slight differences in the relative intensities and frequencies of some bands. In general, the spectrum exhibits a strong characteristic signal at 241 cm^{-1} assigned to the stretching mode of the metal−ligand complex (Ag-Thia). A second very strong band can be seen at 2192 cm^{-1} related with the stretching vibrational mode of the −C≡N moiety. The weak band observed at 1936 cm^{-1} is assigned to the NCN asymmetric stretching mode. This feature will be discussed later and the assignment helped with related published data.[60−62] Around 600 cm^{-1}, it is possible to observe a group of 4 bands with different relative intensities attributed to the vibration of the rings present in Thia. The 591, 610, and 683 cm^{-1} bands are due to vibrations of the 2CPr, while the vibration at 627 cm^{-1} is related to a coupled vibration of both 2CPr and TZDr. Finally, the signals located at 826 and 1109 cm^{-1} are ascribed to the deformation of the 2CPr, while the band at 1446 cm^{-1} is assigned to the deformation of the TZDr. The latter bands have a medium relative intensity. The intensification of bands corresponding to the CIm and TZDr groups and the SERS selection rules[30] allow us to determine that the molecule established a chemical interaction with the surface through the CIm and TZDr groups.

The SERS spectrum of Thia on AgNSt shows strong bands at 260, 605, 685, 817, 930, 1058, 1293, 1327, and 1518 cm^{-1}. The intense and broad band located at 260 cm^{-1} is assigned to the stretching mode of the Ag-Thia complex. Vibrations that are related to the TZDr are observed at 605, 685, 930, 1058, and 1518 cm^{-1}. The assignment of some of these signals (930, 1058, and 1518 cm^{-1}) was performed based on our theoretical calculations because in the above-mentioned work there have been no assignment.[54] The MBm is observed in the SERS spectrum at 1293 and 1327 cm^{-1}, while the 2CPr vibration appears at 817 cm^{-1}. For more details of other bands of the SERS spectra of Figure 4a−d, see Table S2 in the Supporting Information

Resonance Hybrid Allowed by Plasmon. The SERS spectrum of Thia when AgNSp are employed exhibit a band at 1936 cm^{-1} that does not appear in the Raman spectrum. Vibrations in this specific region (1900−2000 cm^{-1}) are not widely explained in detail in the Raman-related literature and has only been ascribed to a stretching mode of allenes or cumulated double bonds of the type >C=C=C<.[55−57] The unique possibility to find an allene or cumulated-like vibration in Thia is around the CIm >C=N−C≡N under many different conformations. Figure 5a shows the resonant
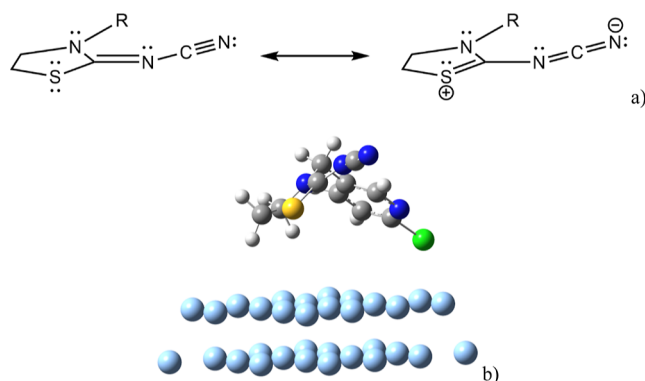
Figure 5. (a) Resonance hybrid for the TZDr-CIm fragment and (b) optimized structure of Thia onto the silver surface.

structures proposed for the TZDr-CIm fragment associated with the mesomeric effect considering the well-known tendency of the cyanamide group to exhibit a resonant structure of the −N=C=N− type. The asymmetric stretching mode of the −N=C=N− moiety can be related to Raman signals appearing in the range 1800−2200 cm^{-1} according to previous works and are attributed to the mentioned resonance.[63−66]

The proposed TZDr-CIm fragment resonance can be supported by the theoretical simulations performed for the Thia and Ag surface-Thia system (Figure 5b). Particularly, the Mulliken charge values for the sulfur atom present in the TZDr (+0.194 in Thia and +0.224 Ag surface-Thia) suggest that this atom may promote the resonance due to its electron-donating nature and high polarizability.

Accordingly, the resonance occurs toward the π-system of the NCN group, where the non-bonding electrons of the amine can delocalize into the π-bonds of the nitrile group.[67] Therefore, the electronic delocalization in the TZDr-CIm moiety is very large due to the high electron-donor capability of the sulfur atom and to the coplanarity of the TZDr with respect to the CIm. According to the theoretical calculations, the resulting dihedral angle between TZDr and CIm is of 4.4°, in agreement with the reported data.[67] Then, it is highly probable that a strong resonance between the latter ring could lead to the appearance of a new SERS band ascribed to an asymmetric N=C=N stretching mode at 1936 cm^{-1}, consistent with related publications.[66,68]

The proposed resonance −S$^{\oplus}$=C(N)−N=C=N$^{\ominus}$ structure is promoted by the interaction of Thia with the metal surface of the AgNSp. On the other hand, this resonance structure is promoted by the lowering of the conformational potential barrier by the metal plasmon. The identification of this structure in the SERS spectrum is a proof of the effect of the metal on the structural change induced on the Thia molecule.

Degradation of Thia by PCh on AgNSt. In general, the enhancement of the Raman spectrum occurs due to the adsorption or approximation of a molecule onto the surface of a noble metal NP. The orientation of the vibrational mode of a functional group or molecular moiety in relation to the surface will allow it to be enhanced (α_{zz} component). This is well explained by the SERS selection rules and is usually used to infer about the orientation of the molecule on a surface.[30] The SERS spectrum often presents several well-defined bands with average widths of 50 cm^{-1} as in the case of Thia onto the
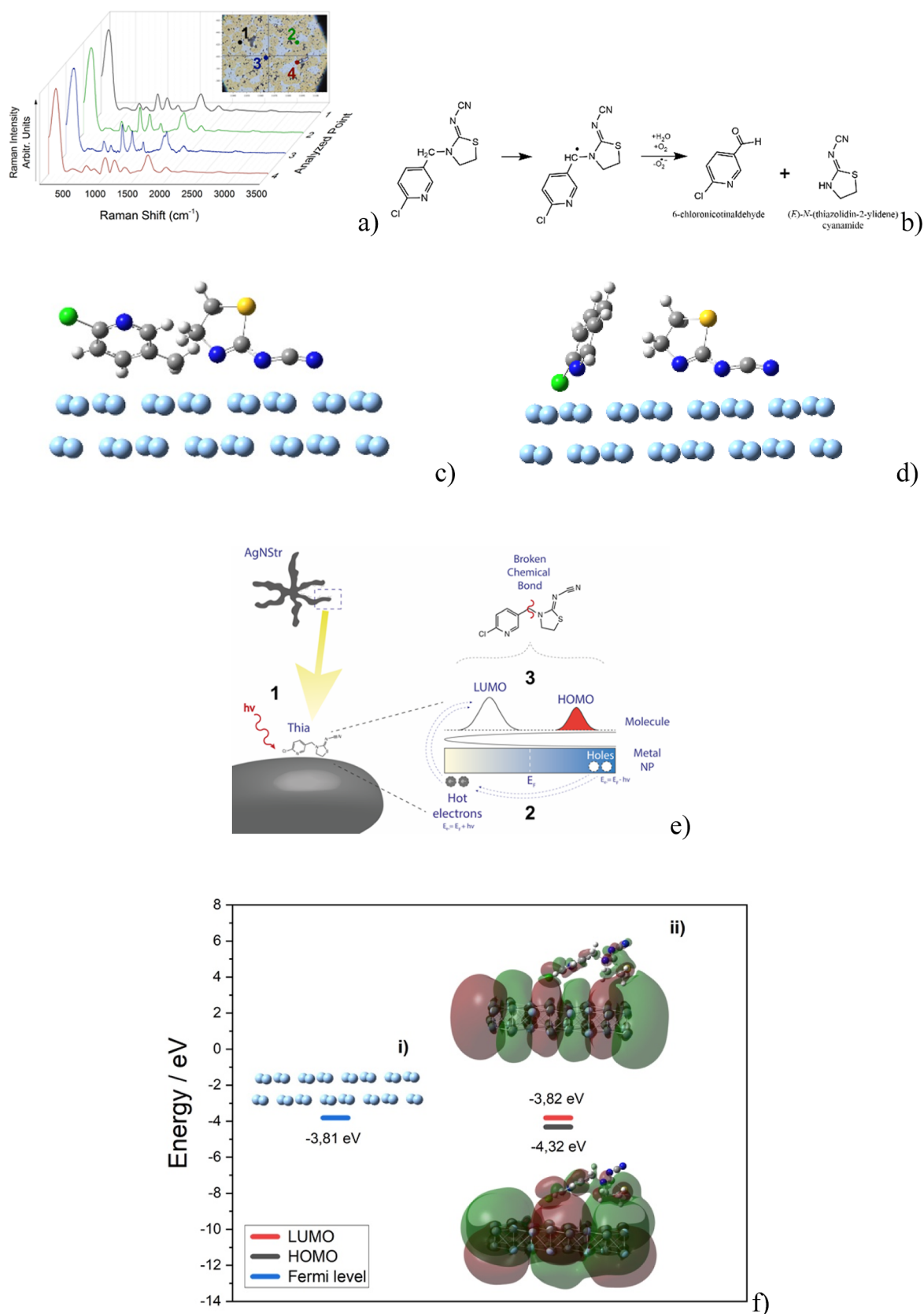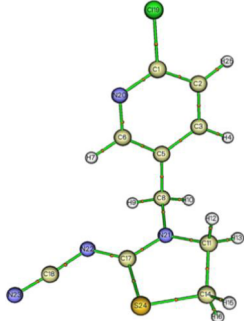
Figure 6. (a) Spectral reproducibility of Thia onto AgNSt. (b) Proposed mechanism to produce two fragments from the Thia structure. (c,d) Orientation of two theoretical simulations. (e) Formation of the TNI to cleavage a bond. (f) Energy representation of the Ag surface/Thia system.

AgNSp. The bandwidths always depend on the molecular system being worked with.

In the SERS spectrum of Thia on AgNSt (see Figure 4a and the reproducibility in Figure 6a), it is possible to observe a few

Table 1. AIM-Based Parameters $\nabla^2\rho$ BCP, LBO, and BDE for Selected Bonds[a]

Bond	$\nabla^2\rho$ BCP (a.u)	LBO	BDE (kcal/mol)	Thia molecule structure
C8-N21	-0.618	0.582	59.226	
C5-C8	-0.586	0.976	86.281	
C17-N22	-0.106	1.313	125.001	
C18-N22	-1.041	1.152	115.859	

[a]Insert: Thia molecular structure.

medium-strong signals with a considerable average bandwidth of 80 cm^{-1}. As can be seen in Figure 4b, a broad band attributed to the metal-adsorbate vibration is observed in this spectrum with a maximum between 250 and 275 cm^{-1}, indicating that chlorine and nitrogen atoms are interacting with the surface. Two medium bands observed at 605 and 685 cm^{-1} ascribed to the stretching mode of C−S give information about the orientation of the TDZr onto the surface, which in this case is tilted. This agrees with other medium bands at 1058 cm^{-1}, attributed to the breathing mode of the TDZr and the signal that appears at 1518 cm^{-1} associated with the stretching of the C=N bond between TDZr and ClM. To complement and support the TZDr orientation, two signals are observed at 1327 and 1293 cm^{-1} related to the vibration of wagging and twisting of the −CH$_2$ of the TDZr.

According to the geometrical position that ClM has in relation to the TDZr, it was expected that the signal of C≡N should not be observed in the spectrum. In this case, the intensity of the stretching mode of the nitrile group is very weak and suffers a red shift from 2184 cm^{-1} in the Raman spectrum to 2113 cm^{-1} in the SERS spectrum onto AgNSt.[69] In addition to this, the deduced parallel orientation is in agreement with the fact that this group (nitrile) is adsorbed via the π-system (or π back-bonding) with AgNSt.[54]

As it was expected due to its orientation, some signals associated with the 2CPr were not enhanced. For example, the breathing modes at 1001 and 1030 cm^{-1} were not observed in the SERS spectrum, and the signal ascribed to the C−H stretching expected around 3060 cm^{-1} was also not observed (see Figure 4d). Based in this spectral evidence for 2CPr, all in-plane vibrations were not enhanced. Conversely, the out-of-plane mode of the C−H deformation in the 2CPr moiety was enhanced, as can be seen in the signal at 817 and 1518 cm^{-1}. This is consistent with the proposed orientation for the 2CPr onto the surface.

On the other hand, two anomalies are observed in the spectrum; a new signal at 1720 cm^{-1} that could be related to the stretching of a carbonyl group,[55] as well as the disappearance of the signal expected around 1440 cm^{-1} assigned to the −CH$_2$− bridge vibration (MBm). These spectral considerations, in addition to (I) the loss and (II) the broadening of signals observed in the SERS profile, lead us to propose the formation of two degradation products derived from 2CPr and TDZr fragments, induced by the influence of

the metal plasmon. The evidence of the resulting degradation species agrees with that proposed in a published work[70] based on the electron transfer mechanism degradation, in which the products are formed as a consequence of the cleavage of the −CH$_2$− bridge (see Figure 6b). Similarly, the −CH$_2$− bridge breaking is proposed in the study of the heterogeneous photocatalysis of Thia by employing a TiO$_2$-based photocatalyst and UV radiation.[71] In this sense, our experimental results complemented with reported studies,[70,71] indicating that it would be possible to obtain as the Thia degradation product an aromatic-aldehyde-like fragment, as it can be seen in the proposed pathway in Figure 6b.In addition to the changes observed in the spectra of Thia in the presence of AgNSt, the theoretical model shows that the nitrile group is not directly interacting with the surface. In this sense, two different simulations were considered by taking into account the homolytic break centered in the C8−N21 bond (see Figure 6c,d); in both cases, after the cleavage, the N−C≡N group of TZDr is adsorbed on the Ag surface.

Based on the described SERS spectrum and considering the high plasmonic activity of the AgNSt, we propose the decomposition of Thia as a direct consequence of the plasmon deactivation through a non-radiative way following the IHET mechanism, were the plasmon-generated hot electrons directly interact with fragments of the molecule adsorbed onto the surface of the AgNSt.[72]

To use the plasmonic properties of a NP, it is necessary to excite it and then take advantage of the deactivation mechanism in a chemical process. The plasmon activation is explained by the mechanism of excitation/deactivation that occurs in three steps according to the deactivation PCh mechanism (see Figure 6e). In the first step (1), the AgNSt absorb the 785 nm laser radiation exciting the LSPRs of the NP, generating the activation of the plasmon activity. Second (2), because of the excitation, a hot electron is promoted to the high-energy Fermi level (EF), leaving a hole in its place. By non-radiative decay, the hot electron with energy equal to EF − $h\nu'$ acquires a higher energy to be promoted to an EF + $h\nu'$ energy level in the metal NP. This hot electron is transferred to the LUMO of Thia to form, in the third step (3), a transient negative ion (TNI) described as an ion that reacts rapidly onto the surface of the NP causing the bond cleavage. To give an estimated approach of the energies involved in this process, in Figure 6f, the theoretical values of EF, HOMO, and LUMO

are presented. The theoretical EF value for a surface consisting of 32 silver atoms is close to reported data.[73,74]

Theoretical calculations were performed in order to determine how the electronic distribution of Thia will be affected by the injection of one electron. To do this, some bonds of Thia were selected according to their significant values for the AIM properties. Without the Ag surface, these selected bonds were checked based on the AIM theory using the Laplacian of the electron density at the bond critical point ($\nabla^2\rho$ BCP)[75] and Laplacian bond order (LBO).[76] Bond dissociation energies (BDE) were also used to establish the main cleavages in Thia.[77] The obtained results are summarized in Table 1.

In addition, HOMO/LUMO analysis was performed by injecting one electron into the LUMO of Thia to verify the TNI presence.

The $\nabla^2\rho$ BCP value can be related to the bond strength. In the case of the C18−N22 bond (imine group of CIm), the $\nabla^2\rho$ BCP exhibits a more negative value in comparison to other selected bonds. This result suggests that this bond has a higher tendency to break. However, this is not in agreement with the experimental data obtained since it is still possible to observe two weak bands at 2113 and 2160 cm^{-1} in the SERS spectrum on AgNSt which corresponds to the vibration of C≡N. Considering the above data, the second most negative value is presented by the C8−N21 bond associated with the MBm.

On the other hand, the LBO value is defined as a covalent bond order based on the Laplacian of electron density ($\nabla^2\rho$) in fuzzy overlap space and has a direct correlation with BDE. The lowest value for this parameter displays the tendency of cleavage for the bonds C5−C8 and C8−N21.

Finally, the BDE of each bond was also calculated to evaluate the feasibility of the homolytic break of each bond. This energy depends on the thermodynamic stability of the formed radicals. According to the calculated BDE values, the C8−N21 bond (followed by the C5−C8 bond) requires less energy than the others (C17−N22 and C18−N22) for its break.

In summary, the BDE and the AIM-based parameters ($\nabla^2\rho$ BCP and LBO) indicate that the most likely homolytic cleavage in Thia occurs at the C8−N21 bond (MBm). This simulation is in complete agreement with the disappearance observed in the SERS spectrum of the band associated with the MBm group at 1440 cm^{-1}.

A relevant aspect to analyze is how the HOMO-to-LUMO transition can provide valuable information about the electronic structure of Thia after the incorporation of one electron. The injection of one electron into the LUMO of Thia from the generated hot electron promotes the stretching and weakening of bonds, leading to the formation of a new species. The new molecular species (denominated TNI) undergoes an energy reduction when it returns to the ground-state potential energy surface, thus resulting in an increase of the vibrational energy. According to a published work, the lifetime of this transition is long enough for the chemical transformation to occur.[78] In fact, this is what it was deduced from the SERS spectra of Thia on the AgNSt surface, further supported by the discussed theoretical bond parameters.

The analysis of molecular orbitals of Thia displays that the HOMO is mainly located at the central MBm, TZDr, and the electron-withdrawing CIm (Figure 7a(i)). Regarding the LUMO, it is possible to observe that is located in the 2CPr moiety (Figure 7a(i)), where is clear that chlorine atom has an
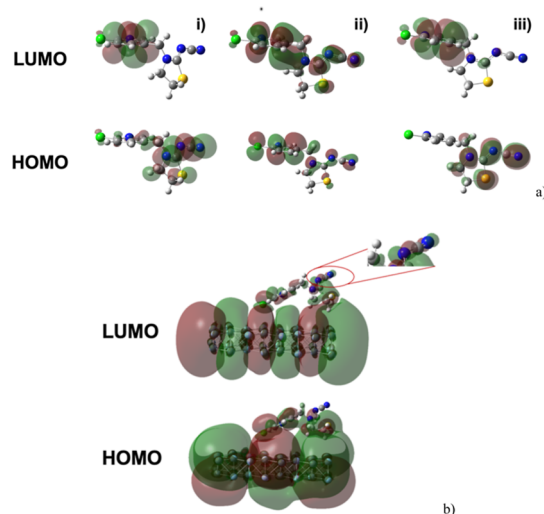
Figure 7. (a) Frontiers molecular orbitals of neutral Thia (i), anionic Thia (ii), and the optimized structure of Thia without extra electrons (iii). (b) Frontiers molecular orbitals of Thia onto the Ag surface. In the red oval is presented the electronic population of the amplified CIm group.

electron acceptor role in the ring. Considering the formation of the TNI, the Thia structure with an additional electron was optimized to observe the electronic distribution in the LUMO (Figure 7a(ii)). This new simulation shows that the LUMO is now located between 2CPr and Cim passing through MBm and TDZr. When this last geometry is optimized without the added extra electron (Figure 7a(iii)), it is possible to see that the HOMO/LUMO locations are like the ones obtained for the original Thia (Figure 7a(i)). This result supports the fact that the electron inclusion in Thia causes a significant change in the electronic structure of the molecule.

Analysis of the HOMO of Thia optimized on the Ag surface (Figure 7b) presents a localized distribution on the surface and on both sides of Thia but not on the CIm group. Contrarily, the LUMO displays that the electronic distribution is also located in the CIm group, which can be interpreted as that Ag NPs inject an electron into Thia and change the electronic distribution. Comparing the LUMO distribution of Thia with an extra electron (Figure 7a(ii)) and Thia onto the Ag surface (Figure 7b), it is possible to support the idea that Thia cleavage occurs due to the C8−N21 weakening bond, which is consistent with the experimental data obtained in the SERS experiments.

■ CONCLUSIONS

AgNSp and AgNSt were successfully synthetized and used to enhance the Raman profile of Thia. Experimental results evidence that (i) 785 nm laser induces an LSPR phenomenon on both AgNSp and AgNSt, which leads to obtaining SERS spectra of Thia, and (ii) the deactivation of the LSPR can induce structural changes in Thia.

Particularly, onto AgNSp, the SERS spectrum presents a new band at 1936 cm^{-1} that was assigned to the asymmetric stretching mode of −N=C=N− derived from a mesomeric effect in the cyanamide (CIm) moiety of Thia. This result was supported by theoretical simulations where it was possible to conclude that the non-bonding electrons of the amine can delocalize into the π-bonds of the nitrile group, generating a large electron delocalization on the TZDr-CIm moiety which

when combined with the plasmonic effect of the NPs leads to a conformational change of Thia.

On the other hand, when AgNSt were used, the SERS spectrum of Thia did not show the band assigned to the $-CH_2-$ bridge vibration, indicating that Thia breakage takes place in the MBm, leading to the formation of two molecular fragments, as well as a new signal at 1720 cm^{-1} that could be related to the stretching of a carbonyl group, evidencing that it would be possible to obtain a Thia degradation product which is an aromatic-aldehyde-like fragment. Theoretical calculations based on DFT and topological parameters described by the AIM theory support the fact that the proposed cleavage over AgNSt occurs in the C8−N21 bond of MBm.

Finally, the difference observed when AgNSt and AgNSp are used is related to the shape of each NP and the energy involved in the plasmonic activity, as it can be seen in the UV−visible spectral results, where at the excitation wavelength used, AgNSt exhibit a higher absorbance than AgNSp and consequently a bigger SPR effect may be induced.

ASSOCIATED CONTENT

SI **Supporting Information**

The Supporting Information is available free of charge at https://pubs.acs.org/doi/10.1021/acsomega.3c01878.

Theoretical/experimental frequencies, scale factors, and assigment for Thiacloprid (PDF)

AUTHOR INFORMATION

Corresponding Author

Freddy Celis − *Laboratorio de Procesos Fotónicos y Electroquímicos, Facultad de Ciencias Naturales y Exactas, Universidad de Playa Ancha, Valparaíso 2360002, Chile;* orcid.org/0000-0003-3195-3018; Phone: +56 32 2205547; Email: freddy.celis@upla.cl

Authors

Andrés Aracena − *Instituto de Ciencias Naturales, Universidad de las Américas, Santiago 7500000, Chile*

Macarena García − *Laboratorio de Procesos Fotónicos y Electroquímicos, Facultad de Ciencias Naturales y Exactas, Universidad de Playa Ancha, Valparaíso 2360002, Chile;* orcid.org/0000-0002-8049-608X

Rodrigo Segura del Río − *Instituto de Química y Bioquímica, Facultad de Ciencias, Universidad de Valparaíso, Valparaíso 2362735, Chile;* orcid.org/0000-0003-0928-0021

Santiago Sanchez-Cortes − *Instituto de Estructura de la Materia, Consejo Superior de Investigaciones Científicas, CSIC, Madrid 28006, Spain;* orcid.org/0000-0002-1081-4644

Patricio Leyton − *Pontificia Universidad Católica de Valparaíso, Instituto de Química, Valparaíso 46383, Chile*

Complete contact information is available at:
https://pubs.acs.org/10.1021/acsomega.3c01878

Author Contributions

F.C. and S.S.C. contributed to experimental aspects, formal analysis, and general investigation. R.S. performed the FESEM analysis and contributed to the review. A.A. contributed to theoretical aspects to the investigation and writing. F.C., M.G., and S.S.C. contributed to writing—review, editing, supervision, and resources. All authors have read and agreed to the published version of the manuscript.

Notes

The authors declare no competing financial interest.

REFERENCES

(1) Hallmann, C. A.; Foppen, R. P. B.; van Turnhout, C. A. M.; de Kroon, H.; Jongejans, E. Declines in Insectivorous Birds Are Associated with High Neonicotinoid Concentrations. *Nature* **2014**, *511*, 341−343.

(2) Keil, A. P.; Daniels, J. L.; Hertz-Picciotto, I. Autism Spectrum Disorder, Flea and Tick Medication, and Adjustments for Exposure Misclassification: The CHARGE (CHildhood Autism Risks from Genetics and Environment) Case-Control Study. *Environ. Health* **2014**, *13*, 3.

(3) Toğay, V. A.; Yavuz Türel, G.; Aşcı Çelik, D.; Özgöçmen, M.; Evgen Tülüceoğlu, E.; Şen, İ.; Ayvaz, Y. DNA Damage Effect of Cyprodinil and Thiacloprid in Adult Zebrafish Gills. *Environ. Sci. Pollut. Res.* **2021**, *28*, 14482−14487.

(4) Fent, K.; Schmid, M.; Hettich, T.; Schmid, S. The Neonicotinoid Thiacloprid Causes Transcriptional Alteration of Genes Associated with Mitochondria at Environmental Concentrations in Honey Bees. *Environ. Pollut.* **2020**, *266*, 115297.

(5) Hong, J.; Kawashima, A.; Okamoto, M.; Hamada, N. Evaluation of Membrane Filtration for Cleanup in Multi-Residue Pesticide Analysis of Spinach. *Food Control* **2017**, *79*, 134−142.

(6) Nikbakht Fini, M.; Madsen, H. T.; Muff, J. The Effect of Water Matrix, Feed Concentration and Recovery on the Rejection of Pesticides Using NF/RO Membranes in Water Treatment. *Sep. Purif. Technol.* **2019**, *215*, 521−527.

(7) Cederlund, H.; Börjesson, E.; Lundberg, D.; Stenström, J. Adsorption of Pesticides with Different Chemical Properties to a Wood Biochar Treated with Heat and Iron. *Water, Air, Soil Pollut.* **2016**, *227*, 203.

(8) Derylo-Marczewska, A.; Blachnio, M.; Marczewski, A. W.; Seczkowska, M.; Tarasiuk, B. Phenoxyacid Pesticide Adsorption on Activated Carbon − Equilibrium and Kinetics. *Chemosphere* **2019**, *214*, 349−360.

(9) Kumar, S.; Kaushik, G.; Dar, M. A.; Nimesh, S.; López-Chuken, U. J.; Villarreal-Chiu, J. F. Microbial Degradation of Organophosphate Pesticides: A Review. *Pedosphere* **2018**, *28*, 190−208.

(10) Zhang, X.; Gao, Y.; Zang, P.; Zhao, Y.; He, Z.; Zhu, H.; Song, S.; Zhang, L. Study on the Simultaneous Degradation of Five Pesticides by Paenibacillus Polymyxa from Panax Ginseng and the Characteristics of Their Products. *Ecotoxicol. Environ. Saf.* **2019**, *168*, 415−422.

(11) Liu, Z.; Tian, Y.; Zhou, X.; Liu, X.; Huang, L. Comparison of Two Different Nickel Oxide Films for Electrochemical Reduction of Imidacloprid. *RSC Adv.* **2020**, *10*, 3040−3047.

(12) Martin, E. T.; McGuire, C. M.; Mubarak, M. S.; Peters, D. G. Electroreductive Remediation of Halogenated Environmental Pollutants. *Chem. Rev.* **2016**, *116*, 15198−15234.

(13) Zhou, Y.; Fan, X.; Zhang, G.; Dong, W. Fabricating MoS2 Nanoflakes Photoanode with Unprecedented High Photoelectrochemical Performance and Multi-Pollutants Degradation Test for Water Treatment. *Chem. Eng. J.* **2019**, *356*, 1003−1013.

(14) Marin, M. L.; Santos-Juanes, L.; Arques, A.; Amat, A. M.; Miranda, M. A. Organic Photocatalysts for the Oxidation of Pollutants and Model Compounds. *Chem. Rev.* **2012**, *112*, 1710−1750.

(15) Gligorovski, S.; Strekowski, R.; Barbati, S.; Vione, D. Environmental Implications of Hydroxyl Radicals (•OH). *Chem. Rev.* **2015**, *115*, 13051−13092.

(16) Legrini, O.; Oliveros, E.; Braun, A. M. Photochemical Processes for Water Treatment. *Chem. Rev.* **1993**, *93*, 671−698.

(17) Acero, J. L.; Real, F. J.; Javier Benitez, F.; Matamoros, E. Degradation of Neonicotinoids by UV Irradiation: Kinetics and Effect of Real Water Constituents. *Sep. Purif. Technol.* **2019**, *211*, 218−226.

(18) González-Mariño, I.; Rodríguez, I.; Rojo, L.; Cela, R. Photodegradation of Nitenpyram under UV and Solar Radiation: Kinetics, Transformation Products Identification and Toxicity Prediction. *Sci. Total Environ.* **2018**, *644*, 995−1005.

(19) Liang, R.; Tang, F.; Wang, J.; Yue, Y. Photo-Degradation Dynamics of Five Neonicotinoids: Bamboo Vinegar as a Synergistic Agent for Improved Functional Duration. *PLoS One* **2019**, *14*, No. e0223708.

(20) Aragay, G.; Pino, F.; Merkoçi, A. Nanomaterials for Sensing and Destroying Pesticides. *Chem. Rev.* **2012**, *112*, 5317−5338.

(21) Rawtani, D.; Khatri, N.; Tyagi, S.; Pandey, G. Nanotechnology-Based Recent Approaches for Sensing and Remediation of Pesticides. *J. Environ. Manage.* **2018**, *206*, 749−762.

(22) Zhang, Z.; Deckert-Gaudig, T.; Singh, P.; Deckert, V. Single Molecule Level Plasmonic Catalysis − a Dilution Study of p-Nitrothiophenol on Gold Dimers. *Chem. Commun.* **2015**, *51*, 3069−3072.

(23) Abd El-Aziz, A. R.; Al-Othman, M. R.; Mahmoud, M. A. Degradation of DDT by Gold Nanoparticles Synthesised Using Lawsonia Inermis for Environmental Safety. *Biotechnol. Biotechnol. Equip.* **2018**, *32*, 1174−1182.

(24) Dissanayake, N. M.; Arachchilage, J. S.; Samuels, T. A.; Obare, S. O. Highly Sensitive Plasmonic Metal Nanoparticle-Based Sensors for the Detection of Organophosphorus Pesticides. *Talanta* **2019**, *200*, 218−227.

(25) Rosbero, T. M. S.; Camacho, D. H. Green Preparation and Characterization of Tentacle-like Silver/Copper Nanoparticles for Catalytic Degradation of Toxic Chlorpyrifos in Water. *J. Environ. Chem. Eng.* **2017**, *5*, 2524−2532.

(26) Tariq, S. R.; Nisar, L. Reductive Transformation of Profenofos with Nanoscale Fe/Ni Particles. *Environ. Monit. Assess.* **2018**, *190*, 123.

(27) Mohagheghian, A.; Karimi, S.-A.; Yang, J.-K.; Shirzad-Siboni, M. Photocatalytic Degradation of Diazinon by Illuminated WO₃ Nanopowder. *Desalin. Water Treat.* **2016**, *57*, 8262−8269.

(28) Xue, J.; Luo, Z.; Li, P.; Ding, Y.; Cui, Y.; Wu, Q. A Residue-Free Green Synergistic Antifungal Nanotechnology for Pesticide Thiram by ZnO Nanoparticles. *Sci. Rep.* **2014**, *4*, 5408.

(29) Díaz, F. J. P.; del Río, R. S.; Rodriguez, P. E. D. S. Plasmonic Photocatalysts for Water Splitting. In *Photoelectrochemical Hydrogen Generation: Theory, Materials Advances, and Challenges*; Kumar, P., Devi, P., Eds.; Springer Nature Singapore: Singapore, 2022; pp 117−173.

(30) Moskovits, M. Surface Selection Rules. *J. Chem. Phys.* **1982**, *77*, 4408−4416.

(31) Cortés, E. Activating Plasmonic Chemistry. *Science* **2018**, *362*, 28−29.

(32) Zhan, C.; Chen, X.-J.; Yi, J.; Li, J.-F.; Wu, D.-Y.; Tian, Z.-Q. From Plasmon-Enhanced Molecular Spectroscopy to Plasmon-Mediated Chemical Reactions. *Nat. Rev. Chem.* **2018**, *2*, 216−230.

(33) Stefancu, A.; Nan, L.; Zhu, L.; Chis, V.; Bald, I.; Liu, M.; Leopold, N.; Maier, S. A.; Cortes, E. Controlling Plasmonic Chemistry Pathways through Specific Ion Effects. *Adv. Opt. Mater.* **2022**, *10*, 2200397.

(34) Boerigter, C.; Aslam, U.; Linic, S. Mechanism of Charge Transfer from Plasmonic Nanostructures to Chemically Attached Materials. *ACS Nano* **2016**, *10*, 6108−6115.

(35) Sun, M.; Zhang, Z.; Kim, Z. H.; Zheng, H.; Xu, H. Plasmonic Scissors for Molecular Design. *Chem.—Eur. J.* **2013**, *19*, 14958−14962.

(36) van Schrojenstein Lantman, E. M.; Deckert-Gaudig, T.; Mank, A. J. G.; Deckert, V.; Weckhuysen, B. M. Catalytic Processes Monitored at the Nanoscale with Tip-Enhanced Raman Spectroscopy. *Nat. Nanotechnol.* **2012**, *7*, 583−586.

(37) Ding, Q.; Chen, M.; Fang, Y.; Zhang, Z.; Sun, M. Plasmon-Driven Diazo Coupling Reactions of p -Nitroaniline via −NH 2 or −NO 2 in Atmosphere Environment. *J. Phys. Chem. C* **2017**, *121*, 5225−5231.

(38) Zhang, Q.; Wang, H. Mechanistic Insights on Plasmon-Driven Photocatalytic Oxidative Coupling of Thiophenol Derivatives: Evidence for Steady-State Photoactivated Oxygen. *J. Phys. Chem. C* **2018**, *122*, 5686−5697.

(39) Zhang, Z.; Sheng, S.; Zheng, H.; Xu, H.; Sun, M. Molecular Resonant Dissociation of Surface-Adsorbed Molecules by Plasmonic Nanoscissors. *Nanoscale* **2014**, *6*, 4903−4908.

(40) Kazuma, E.; Jung, J.; Ueba, H.; Trenary, M.; Kim, Y. STM Studies of Photochemistry and Plasmon Chemistry on Metal Surfaces. *Prog. Surf. Sci.* **2018**, *93*, 163−176.

(41) Segura, R.; Vásquez, G.; Colson, E.; Gerbaux, P.; Frischmon, C.; Nesic, A.; García, D. E.; Cabrera-Barjas, G. Phytostimulant properties of highly stable silver nanoparticles obtained with saponin extract from *Chenopodium quinoa. J. Sci. Food Agric.* **2020**, *100*, 4987−4994.

(42) Sharma, R. K.; Yadav, S.; Dutta, S.; Kale, H. B.; Warkad, I. R.; Zboril, R.; Varma, R. S.; Gawande, M. B. Silver Nanomaterials: Synthesis and (Electro/Photo) Catalytic Applications. *Chem. Soc. Rev.* **2021**, *50*, 11293−11380.

(43) Yang, C.; Xie, Y. T.; Yuen, M. M. F.; Xiong, X.; Wong, C. P. A Facile Chemical Approach for Preparing a SERS Active Silver Substrate. *Phys. Chem. Chem. Phys.* **2010**, *12*, 14459−14461.

(44) Xu, Y.; Cao, M.; Zhang, Q. Recent Advances and Perspective on Heterogeneous Catalysis Using Metals and Oxide Nanocrystals. *Mater. Chem. Front.* **2021**, *5*, 151−222.

(45) Celis, F.; Tirapegui, C.; García, M.; Aracena, A.; Aliaga, Á. E.; Campos-Vallette, M. Identification of Coexisting Indigo Species in an Ancient Green Thread Using Direct Plasmon-Enhanced Raman Spectroscopy. *J. Chil. Chem. Soc.* **2020**, *65*, 4798−4803.

(46) Celis, F.; Segura, C.; Gómez-Jeria, J. S.; Campos-Vallette, M.; Sanchez-Cortes, S. Analysis of Biomolecules in Cochineal Dyed Archaeological Textiles by Surface-Enhanced Raman Spectroscopy. *Sci. Rep.* **2021**, *11*, 6560.

(47) Leopold, N.; Lendl, B. A New Method for Fast Preparation of Highly Surface-Enhanced Raman Scattering (SERS) Active Silver Colloids at Room Temperature by Reduction of Silver Nitrate with Hydroxylamine Hydrochloride. *J. Phys. Chem. B* **2003**, *107*, 5723−5727.

(48) Garcia-Leis, A.; Rivera-Arreba, I.; Sanchez-Cortes, S. Morphological Tuning of Plasmonic Silver Nanostars by Controlling the Nanoparticle Growth Mechanism: Application in the SERS Detection of the Amyloid Marker Congo Red. *Colloids Surf., A* **2017**, *535*, 49−60.

(49) Frisch, M. J.; Trucks, G. W.; Schlegel, H. B.; Scuseria, G. E.; Robb, M. A.; Cheeseman, J. R.; Scalmani, G.; Barone, v.; Mennucci, B.; Petersson, G. A.; Nakatsuji, H.; Caricato, M.; Li, X.; Hratchian, H. P.; Izmaylov, A. F.; Bloino, J.; Zheng, G.; Sonnenberg, J. L.; Hada, M.; Ehara, M.; Toyota, K.; Fukuda, R.; Hasegawa, J.; Ishida, M.; Nakajima, T.; Honda, Y.; Kitao, O.; Nakai, H.; Vreven, T.; Montgomery, J. A., Jr.; Peralta, J. E.; Ogliaro, F.; Bearpark, M.; Heyd, J. J.; Brothers, E.; Kudin, K. N.; Staroverov, v. N.; Kobayashi, R.; Normand, J.; Raghavachari, K.; Rendell, A.; Burant, J. C.; Iyengar, S. S.; Tomasi, J.; Cossi, M.; Rega, N.; Millam, J. M.; Klene, M.; Knox, J. E.; Cross, J. B.; Bakken, v.; Adamo, C.; Jaramillo, J.; Gomperts, R.; Stratmann, R. E.; Yazyev, O.; Austin, A. J.; Cammi, R.; Pomelli, C.; Ochterski, J. W.; Martin, R. L.; Morokuma, K.; Zakrzewski, v. G.; Voth, G. A.; Salvador, P.; Dannenberg, J. J.; Dapprich, S.; Daniels, A.

D.; Farkas, Ö.; Foresman, J. B.; Ortiz, J. V.; Cioslowski, J.; Fox, D. J. *Gaussian 09*. Revision E.01.

(50) Gao, J.-S.; Qiao, J.; Yu, Y.-H.; Hou, G.-F. (Z)-N-{3-[(6-Chloropyridin-3-yl)methyl]-1,3-thiazolidin-2-ylidene}cyanamide. *Acta Crystallogr., Sect. E: Struct. Rep. Online* **2011**, *67*, o1140.

(51) Foresman, J. B.; Frisch, J. *Exploring Chemistry with Electronic Structure Methods*, 3rd ed.; Foresman, J. B., Frisch, A., Eds.; Gaussian, Inc.: Wallingford, CT, 2015.

(52) Legler, C. R.; Brown, N. R.; Dunbar, R. A.; Harness, M. D.; Nguyen, K.; Oyewole, O.; Collier, W. B. Scaled Quantum Mechanical Scale Factors for Vibrational Calculations Using Alternate Polarized and Augmented Basis Sets with the B3LYP Density Functional Calculation Model. *Spectrochim. Acta, Part A* **2015**, *145*, 15−24.

(53) Lu, T.; Chen, F. Multiwfn: A Multifunctional Wavefunction Analyzer. *J. Comput. Chem.* **2012**, *33*, 580−592.

(54) Cañamares, M. V.; Feis, A. Surface-Enhanced Raman Spectra of the Neonicotinoid Pesticide Thiacloprid. *J. Raman Spectrosc.* **2013**, *44*, 1126−1135.

(55) Socrates, G. *Infrared and Raman Characteristic Group Frequencies: Tables and Charts*, 3rd ed.; John Wiley & Sons, Ltd: Chichester, 2004.

(56) Colthup, N. B.; Daly, L. H.; Wiberley, S. E. *Introduction to Infrared and Raman Spectroscopy*, 3rd ed.; Academic Press: San Diego, 1990.

(57) Lin-Vien, D.; Colthup, N. B.; Fateley, W. G.; Grasselli, J. G. *The Handbook of Infrared and Raman Characteristic Frequencies of Organic Molecules*, 1st ed.; Academic Press: London, 1991.

(58) Garcia-Leis, A.; Garcia-Ramos, J. V.; Sanchez-Cortes, S. Silver Nanostars with High SERS Performance. *J. Phys. Chem. C* **2013**, *117*, 7791−7795.

(59) Smitha, S. L.; Nissamudeen, K. M.; Philip, D.; Gopchandran, K. G. Studies on Surface Plasmon Resonance and Photoluminescence of Silver Nanoparticles. *Spectrochim. Acta, Part A* **2008**, *71*, 186−190.

(60) Birk, M.; Winnewisser, M. The Rotation-Vibration Spectrum of Gaseous Cyanamide (H2NCN). *Chem. Phys. Lett.* **1986**, *123*, 382−385.

(61) Carey, F. A.; Sundberg, R. J. *Advanced Organic Chemistry. Part A: Structure and Mechanism*, 5th ed.; Springer US: Boston, MA, 2007.

(62) Tao, F. M.; Klemperer, W.; McCarthy, M. C.; Gottlieb, C. A.; Thaddeus, P. An Ab Initio Study of the HNCN Radical. *J. Chem. Phys.* **1994**, *100*, 3691−3694.

(63) Brown, F. B.; Fletcher, W. H. The Vibrational Spectrum of Dimethyl Cyanamide. *Spectrochim. Acta* **1963**, *19*, 915−923.

(64) Crutchley, R. J.; Naklicki, M. L. Pentaammineruthenium(III) Complexes of Neutral and Anionic (2,3-Dichlorophenyl)Cyanamide: A Spectroscopic Analysis of Ligand to Metal Charge-Transfer Spectra. *Inorg. Chem.* **1989**, *28*, 1955−1958.

(65) Dong, Y.; DiSalvo, F. J. Single Crystal Structure and Raman Spectrum of Ba3Na2(CN2)4. *J. Solid State Chem.* **2006**, *179*, 1363−1368.

(66) Kurzer, F.; Douraghi-Zadeh, K. Advances in the Chemistry of Carbodiimides. *Chem. Rev.* **1967**, *67*, 107−152.

(67) Crutchley, R. Phenylcyanamide Ligands and Their Metal Complexes. *Coord. Chem. Rev.* **2001**, *219−221*, 125−155.

(68) Clark, W. P.; Niewa, R. Synthesis and Characterisation of the Nitridocuprate(I) Nitride Carbodiimide (Sr6N)[CuN2] [CN2]2. *Z. Anorg. Allg. Chem.* **2020**, *646*, 114−119.

(69) Boo, D. W.; Kim, K.; Kim, M. S. Surface-Enhanced Raman Scattering(SERS) of Benzylcyanide in Silver Sol. *Bull. Korean Chem. Soc.* **1988**, *9*, 27−29.

(70) Yin, K.; Deng, Y.; Liu, C.; He, Q.; Wei, Y.; Chen, S.; Liu, T.; Luo, S. Kinetics, Pathways and Toxicity Evaluation of Neonicotinoid Insecticides Degradation via UV/Chlorine Process. *Chem. Eng. J.* **2018**, *346*, 298−306.

(71) Náfrádi, M.; Hlogyik, T.; Farkas, L.; Alapi, T. Comparison of the Heterogeneous Photocatalysis of Imidacloprid and Thiacloprid − Reaction Mechanism, Ecotoxicity, and the Effect of Matrices. *J. Environ. Chem. Eng.* **2021**, *9*, 106684.

(72) Kazuma, E.; Kim, Y. Mechanistic Studies of Plasmon Chemistry on Metal Catalysts. *Angew. Chem., Int. Ed.* **2019**, *58*, 4800−4808.

(73) Stefancu, A.; Lee, S.; Zhu, L.; Liu, M.; Lucacel, R. C.; Cortés, E.; Leopold, N. Fermi Level Equilibration at the Metal-Molecule Interface in Plasmonic Systems. *Nano Lett.* **2021**, *21*, 6592−6599.

(74) Holmberg, N.; Laasonen, K.; Peljo, P. Charge Distribution and Fermi Level in Bimetallic Nanoparticles. *Phys. Chem. Chem. Phys.* **2016**, *18*, 2924−2931.

(75) Matta, C. F.; Boyd, R. J. *The Quantum Theory of Atoms in Molecules: From Solid State to DNA and Drug Design*; Wiley-VCH Verlag GmbH & Co. KGaA: Weinheim, Germany, 2007; pp I−XXXVIII.

(76) Lu, T.; Chen, F. Bond Order Analysis Based on the Laplacian of Electron Density in Fuzzy Overlap Space. *J. Phys. Chem. A* **2013**, *117*, 3100−3108.

(77) St John, P. C.; Guan, Y.; Kim, Y.; Kim, S.; Paton, R. S. Prediction of Organic Homolytic Bond Dissociation Enthalpies at near Chemical Accuracy with Sub-Second Computational Cost. *Nat. Commun.* **2020**, *11*, 2328.

(78) Linic, S.; Christopher, P.; Ingram, D. B. Plasmonic-Metal Nanostructures for Efficient Conversion of Solar to Chemical Energy. *Nat. Mater.* **2011**, *10*, 911−921.